



Measurement of the D^* longitudinal polarization in $B^0 \rightarrow D^{*-} \tau^+ \nu_\tau$ decays

LHCb collaboration[†]

Abstract

The longitudinal polarization fraction of the D^* meson is measured in $B^0 \rightarrow D^{*-} \tau^+ \nu_\tau$ decays, where the τ lepton decays to three charged pions and a neutrino, using proton-proton collision data collected by the LHCb experiment at center-of-mass energies of 7, 8 and 13 TeV and corresponding to an integrated luminosity of 5 fb^{-1} . The D^* polarization fraction $F_L^{D^*}$ is measured in two q^2 regions, below and above $7 \text{ GeV}^2/c^4$, where q^2 is defined as the squared invariant mass of the $\tau \nu_\tau$ system. The $F_L^{D^*}$ values are measured to be $0.52 \pm 0.07 \pm 0.04$ and $0.34 \pm 0.08 \pm 0.02$ for the lower and higher q^2 regions, respectively. The first uncertainties are statistical and the second systematic. The average value over the whole q^2 range is:

$$F_L^{D^*} = 0.41 \pm 0.06 \pm 0.03.$$

These results are compatible with the Standard Model predictions.

Published in Phys. Rev. D 110 (2024) 9, 092007

© 2024 CERN for the benefit of the LHCb collaboration. CC BY 4.0 licence.

[†]Authors are listed at the end of this paper.

1 Introduction

Semileptonic decays of B mesons into final states with a τ lepton are a useful test of the Standard Model (SM) and its extensions. This paper focuses on the $B^0 \rightarrow D^{*-} \tau^+ \nu_\tau$ decay,¹ which is theoretically well understood [1] and is sensitive to new physics (NP) contributions [2]. This decay mode has been studied by both the BaBar and Belle experiments [3–8] and the LHCb experiment [9–11]. These measurements aimed to determine the distributions of the most relevant kinematic variables, such as the τ polarization, the branching fraction and the ratio $\mathcal{R}(D^{(*)}) = \mathcal{B}(B^0 \rightarrow D^{(*)-} \tau^+ \nu_\tau) / \mathcal{B}(B^0 \rightarrow D^{(*)-} \ell^+ \nu_\ell)$, where ℓ denotes an electron or a muon. The latest LHCb analysis of this decay mode obtained a value of $\mathcal{R}(D^*) = 0.260 \pm 0.015$ (stat) ± 0.016 (syst) ± 0.012 (ext) [12], performed with proton-proton (pp) collision data collected at a center-of-mass energy (\sqrt{s}) of 13 TeV and corresponding to an integrated luminosity of 2 fb^{-1} . The current world average for $\mathcal{R}(D^*)$ is 0.287 ± 0.012 and together with the $\mathcal{R}(D)$ measurement shows a tension with the SM at the level of 3.3 standard deviations (σ) [13]. Studies of the kinematic and angular distributions, such as the longitudinal D^* polarization fraction ($F_L^{D^*}$), can provide additional sensitivity to possible NP scenarios [2]. For example, the $F_L^{D^*}$ value could be enhanced by new scalar operators or suppressed by new tensor operators [14]. At present, the only measurement of $F_L^{D^*}$ was performed by the Belle Collaboration with the result $F_L^{D^*} = 0.60 \pm 0.08$ (stat) ± 0.04 (syst) [15]. This value is compatible with the SM expectations [1, 16, 17]. The most recent theoretical predictions, computed with different model assumptions and QCD calculations, converge to a value in a range between 0.43 and 0.46 [18–23].

This paper presents the first measurement of the longitudinal D^* polarization fraction by the LHCb experiment. It uses a sample of $B^0 \rightarrow D^{*-} \tau^+ \nu_\tau$ decays where the D^{*-} meson decays into the $\bar{D}^0 \pi^-$ final state and the τ^+ lepton decays to three charged pions and a tauonic neutrino, with the potential presence of an additional neutral pion, *i.e.* $\tau^+ \rightarrow \pi^+ \pi^- \pi^+ (\pi^0) \nu_\tau$. The measurement is performed using pp collision data collected by the LHCb experiment during 2011–2012 at $\sqrt{s} = 7$ and 8 TeV (Run 1) and during 2015–2016 at $\sqrt{s} = 13$ TeV (Run 2), corresponding to an integrated luminosity of 3 fb^{-1} and 2 fb^{-1} , respectively. The doubly differential decay rate of $D^{*-} \rightarrow \bar{D}^0 \pi^-$ decays,

$$\frac{1}{\Gamma} \frac{d^2\Gamma}{dq^2 d\cos\theta_D} = a_{\theta_D}(q^2) + c_{\theta_D}(q^2) \cos^2\theta_D, \quad (1)$$

depends on the angular distribution of the decay products through θ_D , the angle between the \bar{D}^0 meson direction and the direction opposite to the B^0 meson in the D^* rest frame. The coefficients of the angular distribution, $a_{\theta_D}(q^2)$ and $c_{\theta_D}(q^2)$, encapsulate the hadronic effects and the fundamental couplings [24] and depend on q^2 , the squared invariant mass of the $\tau\nu_\tau$ system computed as the squared difference between the B and the D^* momenta. The longitudinal polarization $F_L^{D^*}(q^2)$ depends on the angular coefficients as

$$F_L^{D^*}(q^2) = \frac{a_{\theta_D}(q^2) + c_{\theta_D}(q^2)}{3a_{\theta_D}(q^2) + c_{\theta_D}(q^2)} \quad (2)$$

and also depends on q^2 . The q^2 computation is performed correcting the B momentum for the missing neutrinos, achieved by measuring the B and τ line-of-flight vectors² and using

¹The inclusion of charge-conjugate decay modes is implied throughout the paper.

²The line-of-flight vector is the vector pointing from a particle's production vertex to its decay vertex.

the known B and τ masses. The complete reconstruction method was described in detail in Ref. [10]. In this paper, the integrated values of $a_{\theta_D}(q^2)$ and $c_{\theta_D}(q^2)$ in the q^2 region below and above $7 \text{ GeV}^2/c^4$, named simply as a_{θ_D} and c_{θ_D} , are provided. From those, the corresponding integrated $F_L^{D^*}$ values are determined. These results are combined to determine the average integrated values of a_{θ_D} , c_{θ_D} and $F_L^{D^*}$ in the whole q^2 region.

The work described in this paper is organized as follows: the LHCb detector and the simulation are described in Section 2, the event selection is discussed in Section 3, the description of the signal mode is detailed in Section 4, the study of the dominant background components is reported in Section 5, the final fit and the estimation of $F_L^{D^*}$ are discussed in Section 6, the various systematic sources affecting this measurement are listed and described in Section 7, and the final results are given in Section 8.

2 Detector and simulation

The LHCb detector [25, 26] is a single-arm forward spectrometer covering the pseudorapidity range $2 < \eta < 5$, designed for the study of particles containing b or c quarks. The detector includes a high-precision tracking system consisting of a silicon-strip vertex detector surrounding the pp interaction region [27], a large-area silicon-strip detector located upstream of a dipole magnet with a bending power of about 4 Tm, and three stations of silicon-strip detectors and straw drift tubes [28, 29] placed downstream of the magnet. The tracking system provides a measurement of the momentum, p , of charged particles with a relative uncertainty that varies from 0.5% at low momentum to 1.0% at 200 GeV/ c . The minimum distance of a track to a primary pp collision vertex (PV), the impact parameter, is measured with a resolution of $(15 + 29/p_T) \mu\text{m}$, where p_T is the component of the momentum transverse to the beam, in GeV/ c . Different types of charged hadrons are distinguished using information from two ring-imaging Cherenkov detectors [29, 30]. Photons, electrons and hadrons are identified by a calorimeter system consisting of scintillating-pad and preshower detectors, an electromagnetic calorimeter and a hadronic calorimeter. Muons are identified by a system composed of alternating layers of iron and multiwire proportional chambers [29, 31]. The online event selection is performed by a trigger [29, 32], which consists of a hardware stage, based on information from the calorimeter and muon systems, followed by a software stage, which applies a full event reconstruction.

At the hardware trigger stage, events are required to have a muon with high p_T or a hadron, photon or electron with high transverse energy in the calorimeters. For hadrons, the typical transverse energy threshold is 3.5 GeV. The software trigger requires a two-, three- or four-track secondary vertex with a significant displacement from any primary pp interaction vertex. At least one charged particle must have a transverse momentum $p_T > 1.6 \text{ GeV}/c$ and be inconsistent with originating from a PV. A multivariate algorithm [33, 34] is used for the identification of secondary vertices consistent with the decay of a b hadron.

Simulation is required to model the effects of the detector acceptance and the imposed selection requirements. In the simulation, pp collisions are generated using PYTHIA [35] with a specific LHCb configuration [36]. Decays of unstable particles are described by EVTGEN [37], in which final-state radiation is generated using PHOTOS [38]. The signal events are generated forcing the τ lepton to decay in the $3\pi\nu_\tau$ and $3\pi\pi^0\nu_\tau$ final states

using the resonance chiral Lagrangian model [39] modeled with the TAUOLA [40] package, tuned according to the results from the BaBar Collaboration [41]. The interaction of the generated particles with the detector, and its response, are implemented using the GEANT4 toolkit [42] as described in Ref. [43]. The underlying pp interaction is reused multiple times, with an independently generated signal decay for each event [44].

The simulated samples used in this analysis are assigned sets of weights in order to match relevant distributions in the data as closely as possible. These weights account for the $B^0 \rightarrow D^{*-} \tau^+ \nu_\tau$ form factors, the transverse momentum and η distributions of the B meson, the 3π vertex position uncertainty, and, for certain decay modes, the D_s^+ decay model. The weights are determined in the initial phase of the analysis and are included in all the subsequent steps. The effect of the weights is validated through specific control samples, such as the $B^0 \rightarrow D^{*-} \pi^+ \pi^- \pi^+$ decay.

3 Candidate selection

The reconstruction and selection of the $B^0 \rightarrow D^{*-} \tau^+ \nu_\tau$ decays are performed following the same strategy described in Refs. [10, 12]. Each signal candidate is built combining a D^* meson, decaying as $D^{*-} \rightarrow \bar{D}^0 \pi^-$, and a 3π system originating from a common vertex. The 3π vertex is required to be detached from the B^0 vertex due to the lifetime of the τ lepton. This requirement suppresses the large background with the 3π system originating directly from the B^0 decay, referred to as "prompt-decay" background hereafter. Decays of the form $B^0 \rightarrow D^* D_{(s)}^{\pm,0}(X)$, characterized by a signal-like topology, remain the most important background source after this step.

3.1 Event reconstruction and initial selection

An initial selection is applied to suppress the prompt and combinatorial backgrounds. The τ candidates are reconstructed from three tracks, identified as pions, with transverse momentum $p_T > 250$ MeV/ c . Since the 3π vertex is expected to be well separated from the corresponding PV, this distance is required to be 10 times greater than its uncertainty. The radial distance between the 3π vertex and the beam center in the transverse plane is required to be within the range [0.2, 5.0] mm to avoid pion triplets coming from a PV or from secondary interactions.

The D^0 meson, which originates from a D^* meson decay, is reconstructed in the $K^- \pi^+$ mode selecting tracks identified as a kaon and a pion, each with momentum $p > 2$ GeV/ c and transverse momentum $p_T > 250$ MeV/ c . In addition, the kaon-pion system must have an invariant mass in the range [1840, 1890] MeV/ c^2 and have $p_T > 1.2$ GeV/ c . The D^* meson is obtained combining the D^0 candidate and a track, identified as a pion (slow pion), with $p_T > 110$ MeV/ c and selecting only the combinations with a difference between the D^* and D^0 candidate invariant mass in the range [143, 148] MeV/ c^2 . The combinatorial background is further reduced by requiring that the D^0 and the τ candidates originate from the same PV, chosen as the PV that fits best to the flight direction of the B candidate.

The combinations with a D^*-D^0 mass difference or a D^0 mass outside the specified ranges are used to study the combinatorial background, as discussed in Section 5. Finally the B^0 events are built from the combination of the D^* and the τ candidates.

Table 1: List of all the requirements included in the signal selection.

Variable	Requirement
p_T of τ decay product	$> 250 \text{ MeV}/c$
$[z(3\pi) - z(\text{PV})]/\text{error}$	> 10
Radial distance 3π system	$[0.2, 5.0] \text{ mm}$
$m(3\pi)$	$< 1600 \text{ MeV}/c^2$
p of D^0 decay product	$> 2 \text{ GeV}/c$
p_T of D^0 decay product	$> 250 \text{ MeV}/c$
$m(K\pi)$	$[1840, 1890] \text{ MeV}/c^2$
p_T of the D^0 meson	$> 1.2 \text{ GeV}/c$
p_T of the slow pion	$> 110 \text{ MeV}/c$
$\Delta m = m(K\pi\pi) - m(K\pi)$	$[143, 148] \text{ MeV}/c^2$
$m(D^*3\pi)$	$< 5100 \text{ MeV}/c^2$
$\text{PV}(K\pi)$	$= \text{PV}(3\pi)$

To suppress the background in which a kaon is misidentified as a pion or vice versa, all the kaon and pion candidates are required to be correctly identified using information provided by the particle identification (PID) system. The chosen requirements were already studied and applied in the previous LHCb analyses [10, 12] which were proven to be effective in rejecting background sources like $B^0 \rightarrow D^{*-}D^+(X)$, where the D^+ decays as $D^+ \rightarrow K^-\pi^+\pi^+(\pi^0)$.

Finally, because of the presence of neutrinos in the final state, the invariant mass of the $D^*3\pi$ system is required to be below $5100 \text{ MeV}/c^2$ while the τ candidate is required to have an invariant mass lower than $1600 \text{ MeV}/c^2$, in order to suppress a fraction of double-charm background. A full list of all the requirements described in this section is reported in Table 1.

The resolution of the $\cos\theta_D$ variable is determined using a simulated sample of $B^0 \rightarrow D^{*-}\tau^+\nu_\tau$ decays and looking at the distribution of $(\cos\theta_D^{\text{reco}} - \cos\theta_D^{\text{true}})/\cos\theta_D^{\text{true}}$, where $\cos\theta_D^{\text{reco}}$ and $\cos\theta_D^{\text{true}}$ stand for the reconstructed and generated $\cos\theta_D$ value, respectively. The resulting distribution is centered on zero with a standard deviation of 0.57.

3.2 Vertex detachment requirements

The prompt candidates represent the dominant source of background. The baseline strategy for removing this background is to select only the candidates where the distance between the B^0 and the 3π vertices along the beam direction [$\Delta z \equiv z(3\pi) - z(B^0)$] is larger than 4 times its uncertainty ($\sigma_{\Delta z}$). This requirement rejects 99.95% of the prompt background in the Run 1 data sample. In Run 2 data the rejection is lower (around 90%) due to the larger uncertainty on the vertex reconstruction,³ which increased by a relative 10% with respect to the Run 1 value. In order to compensate for this uncertainty degradation, a multivariate algorithm, based on a boosted decision tree (BDT) [45, 46], is trained with the TMVA package integrated in ROOT [47] taking as input the positions

³The larger uncertainty on the vertex reconstruction in Run 2 data is due to radiation damage in the Vertex-Locator during the first LHC running period.

of the D^0 , B^0 and 3π vertices, their corresponding uncertainties, the invariant mass of the 3π system and the angle between the τ momentum and the line of flight from the τ origin to the decay vertex. In the training phase the signal is represented by the simulated $B^0 \rightarrow D^{*-}\tau^+\nu_\tau$ decay while the background is represented by a simulated $b\bar{b} \rightarrow D^*\pi X$ sample. The final requirements on Δz and the BDT response are optimized on Run 2 data in order to maintain the same prompt background rejection as in the Run 1 data.

3.3 Isolation requirements

After the vertex detachment requirements, the dominant background source arises from the $B \rightarrow D^{*-}D(X)$ modes. These events are typically characterized by the presence of additional final-state charged particles, compared to the signal mode. The main contributions are from the $B^0 \rightarrow D^{*-}D^0K^+$, $B \rightarrow D^{*-}D^+(X)$ and $B \rightarrow D^{*-}D_s^+(X)$ decays where the D^0 meson decays into four charged particles and the D^+ or D_s^+ meson decays into five charged particles. The rejection of this background is based on the strategies used in Refs. [10, 12], which exploit a dedicated algorithm to determine the isolation of each track in the signal decay chain from all the other tracks in the event. This requirement preserves around 80% of the signal candidates while rejecting between 82% and 95% of the various partially reconstructed backgrounds.

3.4 Combinatorial background suppression

After applying the requirements described above, the expected level of combinatorial background in the Run 1 sample is below 1%. In the Run 2 data contamination is higher ($\sim 5\%$), since the average number of particles produced at the PVs is larger due to the increased center-of-mass energy. Therefore, a BDT classifier is trained with the aim to further reduce this background in Run 2. The input variables of the BDT classifier include the transverse momentum, the pseudorapidity, the impact parameter and the vertices of the D^* and τ candidates. A requirement on the BDT output rejects 75% of the remaining combinatorial background while retaining 77% of the signal.

3.5 $B \rightarrow D^{*-}D_s^+(X)$ background suppression

The additional suppression of the $B \rightarrow D^{*-}D_s^+(X)$ background is based on a BDT classifier trained on simulated samples. The input features are related to the different dynamics of the 3π system in τ and D_s^+ decays and the isolation of the final state with respect to neutral particles. An important difference lies in the fact that the $\tau^+ \rightarrow \pi^+\pi^-\pi^+\nu_\tau$ mode decays via the intermediate $a_1(1260)^+$ and $\rho^0\pi^+$ states. On the other hand, the D_s^+ meson decay in the $3\pi(X)$ system mainly occurs via the $\eta \rightarrow \pi^+\pi^-\pi^0$ and $\eta' \rightarrow \eta\pi^+\pi^-$ resonances with just a small contribution from the $Xa_1(1260)^+$ mode, where X stands for a η , η' , K^0 , ω or ϕ resonance. The resulting differences in both the minimum and maximum value of the $\pi^+\pi^-$ invariant mass provide significant discrimination. Furthermore, the performance of the BDT classifier is improved by including isolation variables and the information of the energy deposited in the calorimeter, considering that the D_s^+ decays are often characterized by additional charged and neutral particles in the final state. The training is performed on a sample of simulated $B^0 \rightarrow D^{*-}\tau^+\nu_\tau$ decays as signal proxy and simulated $B \rightarrow D^{*-}D_s^+(X)$ decays for the background. The background rejection is about

40% for a signal efficiency around 97%. The output of the BDT classifier is used as a variable in the final fit because of its importance in discriminating the $B \rightarrow D^{*-} D_s^+(X)$ decays background.

4 Signal description

The $F_L^{D^*}$ value is calculated from the a_{θ_D} and c_{θ_D} parameters extracted from a binned maximum-likelihood fit to data. The fit uses four-dimensional templates in terms of the following variables:

- $\cos \theta_D$: defined in Section 1;
- q^2 : defined in Section 1;
- t_τ : decay time of the τ lepton, taking into account the corrections due to the missing neutrino;
- anti- D_s^+ BDT output: the response of the BDT classifier trained to suppress the background due to the $B \rightarrow D^{*-} D_s^+(X)$ decay, defined in Section 3.5.

The value of $F_L^{D^*}$ is measured in two different q^2 regions, below and above 7 GeV²/c⁴, and considering six bins of $\cos \theta_D$ in each region. The binning scheme for the other two variables differs for the Run 1 and Run 2 samples, due to their different luminosities. The t_τ distribution, covering the range [0, 2] ps, is split into four and six bins for the Run 1 and Run 2 data sets, respectively. Similarly, either six or eight bins are used for the anti- D_s^+ BDT distribution.

The a_{θ_D} and c_{θ_D} parameters are determined by splitting the signal simulated template into two components: one is completely unpolarized while the other is fully polarized. With this separation, the a_{θ_D} and c_{θ_D} parameters become directly proportional to the yields of the unpolarized and polarized components, respectively, as discussed in Section 6.

Weights are assigned to the simulated events such that the decay kinematics follow the Caprini-Lellouch-Neubert (CLN) parametrization of the form factors [48]. This procedure is performed by means of the Hammer tool [49] using the dedicated RooHammerModel [50] interface developed by the LHCb Collaboration.

The simulated signal $\cos \theta_D$ distribution is corrected for the reconstruction and selection efficiency and bin migration due to differences between the generated and reconstructed variables. The reconstruction efficiency correction is determined as the ratio of the generated $\cos \theta_D$ distribution, after the full signal selection, to the corresponding distribution at generation level in bins of generated q^2 ; the bin migration correction is determined as the ratio between the $\cos \theta_D$ distribution in bins of q^2 considering the reconstructed and generated quantities, after the full signal selection. The ratio between these $\cos \theta_D$ distributions is computed with the nonuniform distribution of the events in each bin taken into account.

The signal $\cos \theta_D$ distribution in the two q^2 regions for the unpolarized and polarized components, after applying the full signal selection and the form-factor and correction weights, is depicted in Figure 1 for the Run 2 sample. Similar distributions are obtained also from the Run 1 sample and are used to define the signal probability density functions (PDFs) in the final fit. The reconstruction effect leads to a variation of the average

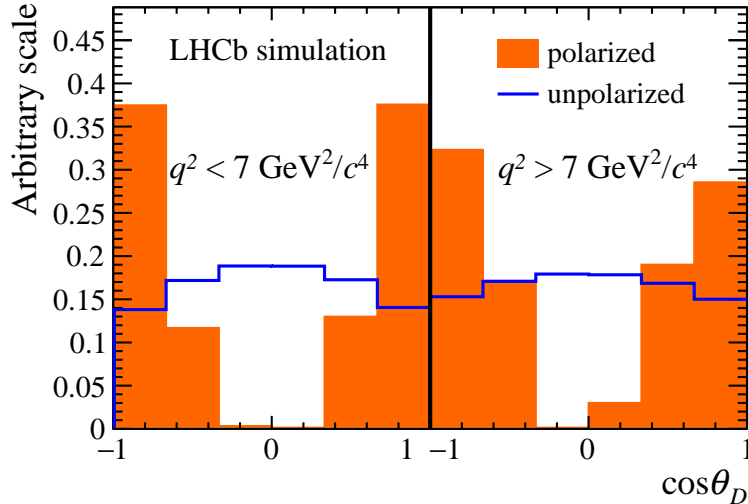


Figure 1: Signal distributions of the $\cos \theta_D$ variable in the two q^2 regions for the unpolarized and polarized components in the Run 2 simulated sample. Similar distributions are calculated for the Run 1 sample. The template for the unpolarized component, which is uniform at generation level, shows clearly the distortion caused by the effect of the reconstruction and the signal selection.

polarization in both the low- and high- q^2 region by a relative 12% and 3%, respectively. Both polarized and unpolarized components are affected by this effect, which is clearly visible in the latter one where the expected flat distribution is distorted.

The total efficiency for the $B^0 \rightarrow D^{*-} \tau^+ \nu_\tau$ mode is estimated from simulation, after corrections are applied. It is evaluated separately for each data-taking period and in each q^2 bin taking into account the effects due to the selection, reconstruction and q^2 bin migration. These efficiencies are used in the final step of the analysis for correcting the observed signal yields when evaluating the $F_L^{D^*}$ value.

5 Background description

After applying the signal selection, the residual background consists mainly of events with a charm hadron decay: $B \rightarrow D^{*-} D(X)$ decays, where D can be, in order of importance, a D_s^+ , D^+ or D^0 meson. PDFs for these background sources are obtained from simulation. The corresponding distributions in Run 1 and Run 2 data are used to validate and correct the simulation. Two different control samples are used to validate the simulated D_s^+ background: the first is based on a pure sample of $D_s^+ \rightarrow \pi^+ \pi^- \pi^+(X)$ decays used to correct the branching fractions relevant to D_s^+ meson production in the generation phase; the second consists of various $B \rightarrow D^{*-} D_s^+(X)$ decays and aims to constrain the relative fractions between these components in the final fit.

5.1 $B \rightarrow D^{*-}(D^+, D^0)(X)$ control sample

The decays $B \rightarrow D^{*-} D^+(X)$ and $B \rightarrow D^{*-} D^0(X)$ can contribute to the background when the D^+ meson decays into two charged pions and a kaon, misidentified as a pion, or when a D^+ or D^0 meson decays into three charged pions and an additional particle.

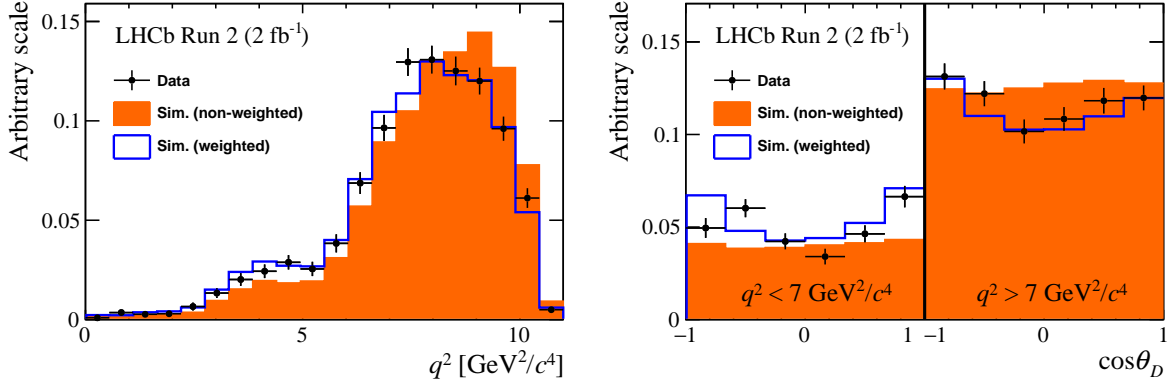


Figure 2: Simulated (left) q^2 and (right) $\cos\theta_D$ distributions for the $B \rightarrow D^{*-}D^0(X)$ control sample before and after the correction for the data-simulation differences in the Run 2 weighted data sample. The $B \rightarrow D^{*-}D^0(X)$ sample is selected using the isolation algorithm to search for an extra kaon around the 3π vertex.

For the $K \rightarrow \pi$ misidentification from D^+ background, a control sample is obtained by inverting the PID requirement on the negatively charged pion and reconstructing the $D^+ \rightarrow K^-\pi^+\pi^+$ decay. For the $D^0 \rightarrow 3\pi X$ background, a control sample is obtained by reconstructing the $D^0 \rightarrow K^-\pi^+\pi^-\pi^+$ decay using the isolation algorithm (described in Section 3.3) to search for the extra kaon around the 3π vertex. In both cases the *sPlot* technique [51] is employed to statistically subtract the combinatorial background and obtain a pure distribution of the decay mode of interest. The q^2 distribution shows some discrepancies between data and simulation due to the imperfect modeling of the inclusive 3π decays. A correction is determined as the ratio of the data and simulated q^2 distributions and is applied to the final templates to account for this effect. Similarly, the $\cos\theta_D$ distribution is not well modeled in the inclusive simulation and is therefore corrected in order to match the one observed in data. The data and simulated q^2 and $\cos\theta_D$ distributions before and after the corrections for the $B \rightarrow D^{*-}D^0(X)$ decays are depicted in Figure 2. Similar distributions are obtained for the $B \rightarrow D^{*-}D^+(X)$ control sample.

5.2 $D_s^+ \rightarrow \pi^+\pi^-\pi^+(X)$ decay model

As mentioned in Section 3.5, the kinematic distributions of the three pions in the final state differ between τ and D_s^+ decays. Special care must be given to D_s^+ decays that have a ρ^0 in the final state, such as the decay through the η' intermediate state and the subsequent $\eta' \rightarrow \rho^0\gamma$ decay, with the following branching fractions: $\mathcal{B}(D_s^+ \rightarrow \eta'X) = (10.3 \pm 1.4)\%$ and $\mathcal{B}(\eta' \rightarrow \rho^0\gamma) = (29.4 \pm 0.4)\%$. This case corresponds to kinematic distributions of the three pions that are similar to those of the signal decays. The aim of the study described in this section is to adjust the branching fractions of the various resonances generated in the simulated samples to better match the data. A dedicated control sample enriched in these decays is used, selected using the same criteria as for the signal selection described in Section 3 but inverting the requirement on the anti- D_s^+ BDT output. The different D_s^+ modes can be separated in three main categories:

- D_s^+ decays where at least one pion comes from an η or η' resonance;

- D_s^+ decays where at least one pion comes from an ω or ϕ resonance;
- D_s^+ decays where the three pions come from the D_s^+ meson with or without an intermediate $a_1(1260)^+$ state: $K^0 3\pi$, $\eta 3\pi$, $\eta' 3\pi$, $\omega 3\pi$, $\phi 3\pi$, $\tau\nu_\tau$ and nonresonant 3π .

The contributions of these $D_s^+ \rightarrow \pi^+\pi^-\pi^+(X)$ decays are estimated from a simultaneous binned maximum-likelihood fit performed on the distribution of four variables: the invariant mass of the 3π system $m(3\pi)$, the mass of the same-charge pions $m(\pi^+\pi^+)$, and the minimum and maximum mass value of the two $\pi^+\pi^-$ combinations $\min[m(\pi^+\pi^-)]$ and $\max[m(\pi^+\pi^-)]$, respectively. The templates of each D_s^+ component are described using the simulated inclusive $B \rightarrow D^{*-}D_s^+(X)$ samples, while the background from non- D_s^+ decays is modeled with the simulated inclusive $b\bar{b} \rightarrow D^*\pi X$ sample. The free parameters of the fit are the total number of D_s^+ events, the fractions of the four resonances η , η' , ω and ϕ , and the relative fractions of the $\eta 3\pi$, $\eta' 3\pi$ and $\omega 3\pi$ decay modes. The parameters related to the other components are constrained or fixed to their values reported in Ref. [52], since their branching fractions are sufficiently well measured. The results of these fits were reported in detail in Refs. [10, 12].

5.3 Constraining the D_s^+ production model

The different $B \rightarrow D^{*-}D_s^+(X)$ decays share similar distributions since the produced excited charm-strange mesons all decay to a D_s^+ and a soft photon or a π^0 and therefore, it is advantageous to constrain their yields in the final fit. Their relative fractions are obtained from a fit to a specific control sample enriched with these decays and then constrained in the final fit. The control sample is obtained applying the same signal selection discussed in Section 3, removing the anti- D_s^+ requirement and the requirement on the maximum B and τ mass values, and requiring the 3π system to have an invariant mass within $20 \text{ MeV}/c^2$ of the known D_s^+ mass value. The surviving events are categorized as the exclusive $B^0 \rightarrow D^{*-}D_s^{*+}$, $B^0 \rightarrow D^{*-}D_s^+$, $B^0 \rightarrow D^{*-}D_{s0}^{*+}$, $B^0 \rightarrow D^{*-}D_{s1}^{*+}$ decays and the inclusive $B^{0,\pm} \rightarrow D^*D_s^+X$ and $B_s^0 \rightarrow D^{*-}D_s^+(X)$ decays, where the first mode is used as normalization.

The q^2 distribution for the exclusive modes peaks exactly at the mass of the $D_s^{(*,**)+}$ states, while the q^2 for the other modes is higher due to the unreconstructed particles in the final state. An extended, binned maximum-likelihood fit is performed to the distribution of the $D^*3\pi$ mass, where the template of each D_s^+ component is taken from the simulation and the distribution of the possible combinatorial background is taken from a data sample obtained by combining D^* and τ candidates with the same sign. The relative fractions extracted from the fit are reported in Table 2 while the fit projections on the fitted and other control variables are shown in Figure 3. The central values and the related uncertainties are included as Gaussian constraints on the various $B \rightarrow D^{*-}D_s^+(X)$ components in the final fit, accounting for the different efficiencies between control and signal samples.

5.4 Other background sources

In addition to the double-charm background, the selected sample is also populated by the combinatorial background and the remnant $B \rightarrow D^*\pi^+\pi^-\pi^+X$ candidates, surviving the vertex-detachment requirement and the requirement on the B mass to be lower than

Table 2: Decay fractions for the $B \rightarrow D^{*-} D_s^+(X)$ decays, normalized for the $B^0 \rightarrow D^{*-} D_s^{*+}$ yield, obtained from the Run 1 and Run 2 control samples.

Parameter	Run 1	Run 2
$f_{B^0 \rightarrow D^{*-} D_s^+}$	0.56 ± 0.05	0.56 ± 0.03
$f_{B^0 \rightarrow D^{*-} D_{s0}^{*+}}$	0.01 ± 0.05	0.08 ± 0.04
$f_{B^0 \rightarrow D^{*-} D_{s1}^{\prime+}}$	0.37 ± 0.05	0.44 ± 0.04
$f_{B^{0,\pm} \rightarrow D^* D_s^+ X}$	0.36 ± 0.07	0.34 ± 0.03
$f_{B_s^0 \rightarrow D^{*-} D_s^+(X)}$	0.07 ± 0.03	0.15 ± 0.04

5100 MeV/ c^2 . Nevertheless, these modes are not expected to affect significantly the signal fit because of their mostly unpolarized $\cos \theta_D$ distribution and the small yield surviving the full signal selection.

6 Signal fit

The number of polarized and unpolarized signal events is estimated from an extended maximum-likelihood fit to the four-dimensional distribution of $\cos \theta_D$, q^2 , t_τ , anti- D_s^+ BDT output. The fit is performed within the SM framework with the free parameters listed below.

- $N_{\text{low } q^2}^{\text{unpol}}$ and $N_{\text{high } q^2}^{\text{unpol}}$: parameters accounting for the number of unpolarized signal events in the low- and high- q^2 regions, respectively.
- $f_{\text{low } q^2}^{\text{pol}}$ and $f_{\text{high } q^2}^{\text{pol}}$: parameters accounting for the fraction of signal polarized events with respect to the number of unpolarized signal events in the low- and high- q^2 regions, respectively.
- $N_{B^0 \rightarrow D^{*-} D^+(X)}$: parameter accounting for the number of $B^0 \rightarrow D^{*-} D^+(X)$ events.
- $f_{B^0 \rightarrow D^{*-} D^0(X)}^{\text{V1V2}}$: free parameter accounting for the fraction of $B^0 \rightarrow D^{*-} D^0(X)$ events where at least one pion comes from a different vertex than the D^0 vertex, with respect to $N_{B^0 \rightarrow D^{*-} D^0(X)}^{\text{same}}$.
- $N_{B^0 \rightarrow D^{*-} D_s^{*+}}$: parameter accounting for the yield of the $B^0 \rightarrow D^{*-} D_s^{*+}$ mode.

To ensure the stability of the fit some parameters are constrained or fixed:

- $f_{\tau^+ \rightarrow \pi^+ \pi^- \pi^+ \pi^0 \nu_\tau}$: fraction of $\tau^+ \rightarrow \pi^+ \pi^- \pi^+ \pi^0 \nu_\tau$ signal events with respect to the $\tau^+ \rightarrow \pi^+ \pi^- \pi^+ \nu_\tau$ mode. This parameter is fixed taking into account the different branching ratios and efficiencies of the two modes.
- $f_{B^0 \rightarrow D^{*-} \tau^+ \nu_\tau}$: fraction of $B^0 \rightarrow D^{*-} \tau^+ \nu_\tau$ decays with respect to the $B^0 \rightarrow D^{*-} \tau^+ \nu_\tau$ signal. This parameter is fixed in the fit to the expected value determined from simulation after correcting the branching fractions used in the generation.⁴

⁴The correction is done by comparing the branching fractions of $B^0 \rightarrow D^{*-} \tau^+ \nu_\tau$ [52] and the theoretical expectations for each D^{**} state from the $R(D^{**})$ predictions reported in Ref. [53].

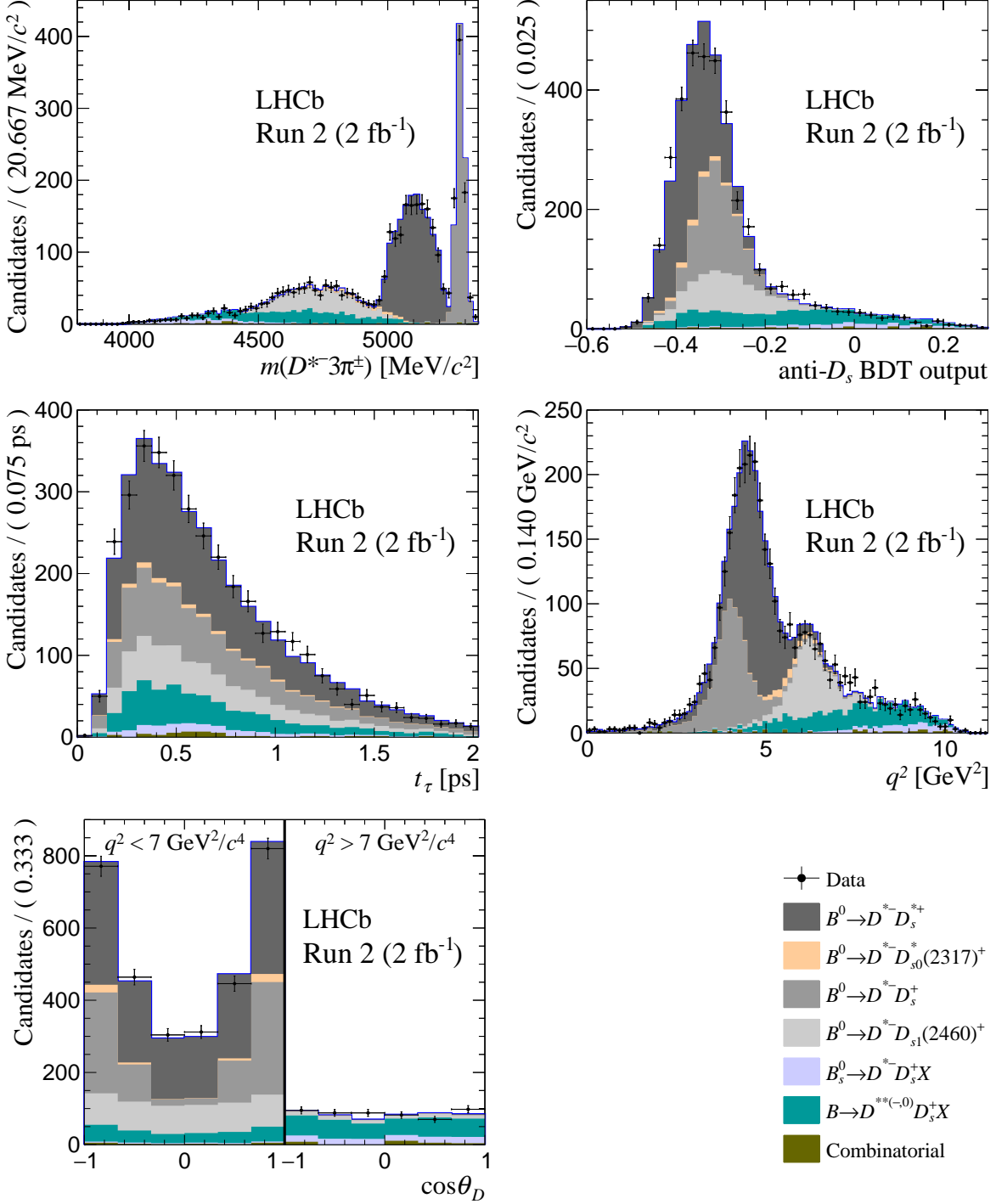


Figure 3: Distribution of the key analysis variables obtained in the $B \rightarrow D^{*-} D_s^+(X)$ enhanced Run 2 data sample with the result of the fit superimposed: (top left) $m(D^* 3\pi)$, (top right) anti- D_s^+ BDT output, (middle left) t_τ , (middle right) q^2 and (bottom) $\cos\theta_D$.

- $f_{B^0 \rightarrow D^{*-} D_{s1}^+}$, $f_{B^0 \rightarrow D^{*-} D_s^+}$, $f_{B^{0,\pm} \rightarrow D^* D_s^+ X}$, $f_{B^0 \rightarrow D^{*-} D_s^+(X)}$ and $f_{B^0 \rightarrow D^{*-} D_{s0}^+}$: set of parameters representing the fraction of the relevant decay mode of interest with respect to the $B^0 \rightarrow D^{*-} D_s^+$ decay. These parameters are constrained to the results of the fit described in Section 5 after correcting for efficiency.

- $N_{B^0 \rightarrow D^{*-} D^0(X)}^{\text{same}}$: number of $B^0 \rightarrow D^{*-} D^0(X)$ events where the three pions in the final state come from the same vertex. This parameter is Gaussian constrained to the number of exclusive $D^0 \rightarrow K^- \pi^+ \pi^- \pi^+$ events recovered by the isolation tool after correcting for the data-simulation differences.
- $N_{B^0 \rightarrow D^{*-} \pi^+ \pi^- \pi^+ X}$: number of prompt $B^0 \rightarrow D^{*-} \pi^+ \pi^- \pi^+ X$ events. The central value is determined from the observed ratio between exclusive $B^0 \rightarrow D^{*-} \pi^+ \pi^- \pi^+$ and the inclusive $B^0 \rightarrow D^{*-} \pi^+ \pi^- \pi^+ X$ decays, corrected for data-simulation differences.
- N_{B1-B2} : number of combinatorial backgrounds where the D^* and the three pions come from different b hadrons. Its value is fixed to the value observed in the wrong-sign sample satisfying the nonisolation and the higher B -mass requirements.
- $N_{\text{fake } D^0}$ and $N_{\text{fake } D^*}$: number of combinatorial background events where a fake D^0 or D^* is reconstructed, respectively. Their value is fixed to the values obtained from a fit to $m(K\pi)$ and $m(K\pi\pi) - m(K\pi)$.

The fractions f^{pol} , $f_{\tau^+ \rightarrow \pi^+ \pi^- \pi^+ \pi^0 \nu_\tau}$ and $f_{B^0 \rightarrow D^{*-} \tau^+ \nu_\tau}$ are assumed to be the same in the Run 1 and Run 2 data samples.

Figure 4 shows the distributions of the variables used in the fit, with a χ^2 per degree of freedom of 806/736. The results are summarized in Table 3. The fractions of polarized signal events are 0.361 ± 0.074 (stat) and 0.013 ± 0.081 (stat) for the low- and high- q^2 regions, respectively. The fit has been repeated on the Run 1 and Run 2 samples separately and no significant discrepancies have been observed in all the parameters.

Table 3: Fit results for the Run 1 and Run 2 data sets.

Parameter	Run 1	Run 2
$N_{\text{low } q^2}^{\text{unpol}}$	360 ± 55	758 ± 62
$N_{\text{high } q^2}^{\text{unpol}}$	532 ± 70	827 ± 109
$f_{\text{low } q^2}^{\text{pol}}$	0.36 ± 0.07	
$f_{\text{high } q^2}^{\text{pol}}$	0.01 ± 0.08	
$f_{\tau^+ \rightarrow \pi^+ \pi^- \pi^+ \pi^0 \nu_\tau}$	0.28	
$f_{B^0 \rightarrow D^{*-} \tau^+ \nu_\tau}$	0.044	
$N_{B^0 \rightarrow D^{*-} D_s^{*+}}$	2087 ± 77	7475 ± 170
$f_{B^0 \rightarrow D^{*-} D_s^{*+}}$	0.38 ± 0.05	0.37 ± 0.04
$f_{B^0 \rightarrow D^{*-} D_s^+}$	0.51 ± 0.03	0.60 ± 0.03
$f_{B^0, \pm \rightarrow D^* D_s^+ X}$	0.83 ± 0.06	0.48 ± 0.05
$f_{B_s^0 \rightarrow D^{*-} D_s^+ (X)}$	0.17 ± 0.03	0.10 ± 0.02
$f_{B^0 \rightarrow D^{*-} D_s^{*+}}$	0.11 ± 0.02	0.02 ± 0.03
$N_{B^0 \rightarrow D^{*-} D^0(X)}^{\text{same}}$	448 ± 22	1039 ± 52
$f_{B^0 \rightarrow D^{*-} D^0(X)}^{\text{V1V2}}$	0.39 ± 0.18	2.26 ± 0.28
$N_{B^0 \rightarrow D^{*-} D^+(X)}$	1747 ± 118	1740 ± 182
$N_{B^0 \rightarrow D^{*-} \pi^+ \pi^- \pi^+ X}$	408 ± 21	2190 ± 33
N_{B1-B2}	197	216
$N_{\text{fake } D^0}$	110	457
$N_{\text{fake } D^*}$	133	533

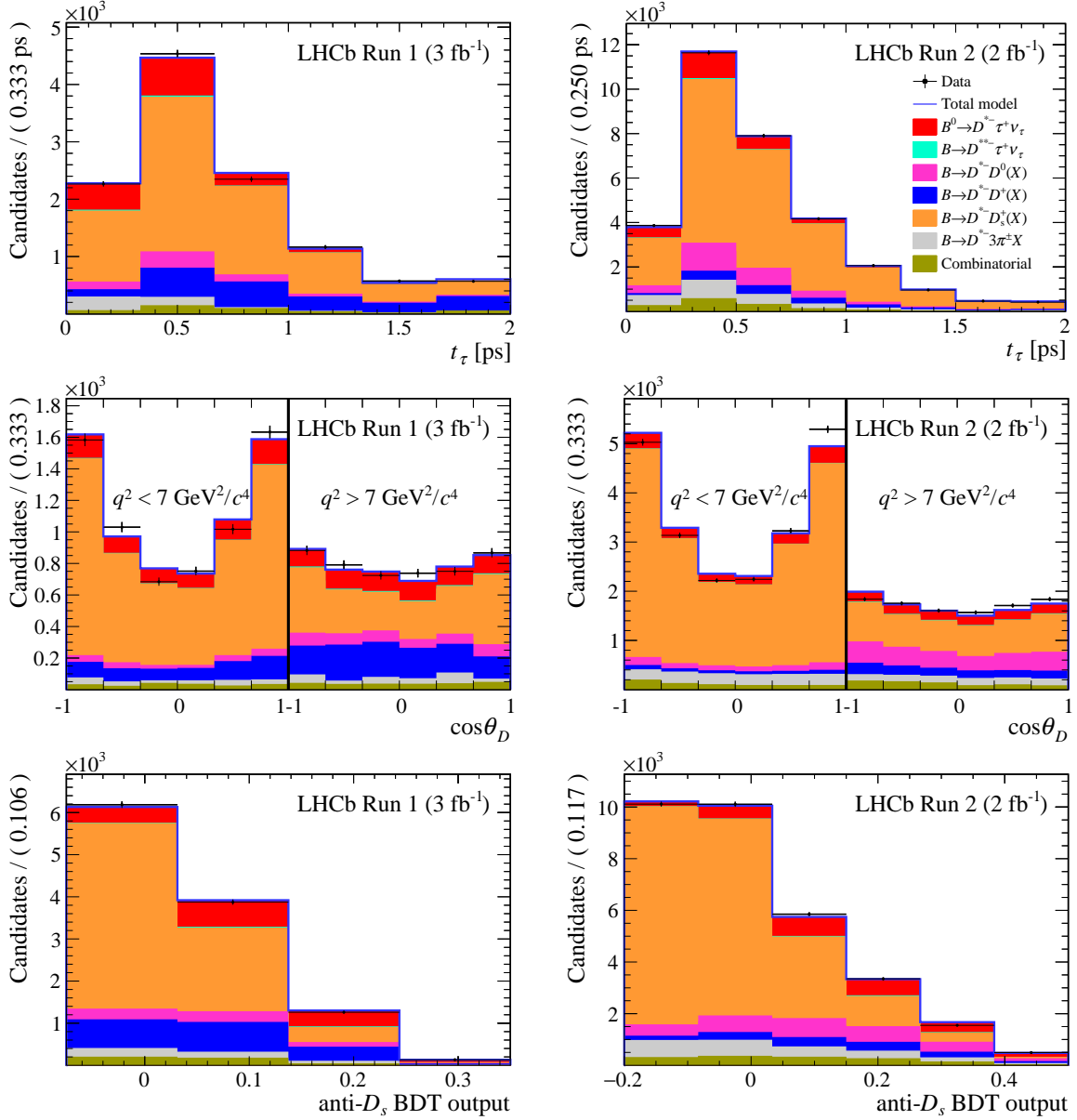


Figure 4: Distributions of the fit variables in the (left) Run 1 and (right) Run 2 data sets with the fit results superimposed.

The observed signal yields are corrected for the efficiency mentioned in Section 4. The a_{θ_D} and c_{θ_D} coefficients of the generated $\cos \theta_D$ distribution are directly related to the efficiency-corrected yields of the polarized and unpolarized signal components in the two q^2 bins. They are determined as

$$a_{\theta_D} = \frac{N_{\text{true}}^{\text{unpol}}}{N_{\text{true}}^{\text{tot}}} \cdot \text{PDF}_{\text{unpol}}|_{\cos \theta_D=0}, \quad c_{\theta_D} = \frac{3}{2} \frac{N_{\text{true}}^{\text{pol}}}{N_{\text{true}}^{\text{tot}}} \Delta, \quad (3)$$

where $\text{PDF}_{\text{unpol}}|_{\cos \theta_D=0}$ represents the value of the unpolarized signal PDF evaluated at 0, Δ is the chosen $\cos \theta_D$ bin width (0.5), the factor $3/2$ arises from the integral of $\cos^2 \theta_D$ distribution, $N_{\text{true}}^{\text{unpol}}$, $N_{\text{true}}^{\text{pol}}$ and $N_{\text{true}}^{\text{tot}}$ are the efficiency-corrected signal yields for the unpolarized, polarized and the total PDFs, respectively, and we consider both Run 1

and Run 2 samples. The corresponding $F_L^{D^*}$ value over the whole q^2 region is determined as the weighted average of the two $F_L^{D^*}$ values, using the efficiency-corrected signal yield in each q^2 bin as weight. The extracted $F_L^{D^*}$, a_{θ_D} and c_{θ_D} values for the binned and total q^2 regions are reported in Table 4.

7 Systematic uncertainties

The main contributions to the systematic uncertainty are due to the signal selection requirements, q^2 bin migration, signal and background modeling, and limited size of the simulated samples. A breakdown of the systematic uncertainties is reported in Table 5 while in the following a brief description is provided for each source.

The simulated signal distributions are weighted according to the form-factor values predicted by the CLN parametrization. Two systematic uncertainties are assigned due to limited knowledge of the form factors: *FF parameters* is evaluated varying the CLN parameters within their uncertainties, while *FF model* is determined repeating the fit with the Boyd-Grinstein-Lebed parametrization [54, 55].

The effects of the *signal selection* and the *q^2 bin migration* on the signal $\cos\theta_D$ template are also considered. A systematic uncertainty is assigned varying these two corrections within their statistical uncertainties. The presence of any bias in the fit procedure is assessed repeating the fit on a set of pseudoexperiments, obtained with a bootstrap technique from the data distribution (*Fit validation*). The $F_L^{D^*}$ value used in the generation of the simulated signal sample (*$F_L^{D^*}$ in simulation*) can introduce a bias in the reconstruction efficiency and acceptance in the $\cos\theta_D$ distribution. Different $F_L^{D^*}$ hypotheses are considered in the $F_L^{D^*}$ range [0.33, 1.0] obtaining each time a new set of signal templates. The fit is repeated and a systematic uncertainty is assigned as the maximum difference with respect to the default $F_L^{D^*}$ values.

The fraction of $\tau^+ \rightarrow \pi^+\pi^-\pi^+\pi^0\nu_\tau$ ($f_{\tau^+\rightarrow\pi^+\pi^-\pi^+\pi^0\nu_\tau}$) decays is fixed in the signal fit so a systematic uncertainty is assigned repeating the fit and varying the central value according to its uncertainty. A similar strategy is used for the quantity $f_{B^0\rightarrow D^{*-}\tau^+\nu_\tau}$, constraining the ratio between the $B^0 \rightarrow D^{*-}\tau^+\nu_\tau$ events and the signal decay (*Fraction of D^{*-} feed-down*).

The D_s^+ decays in simulation are corrected by the weights obtained in the fit to the $D_s^+ \rightarrow \pi^+\pi^-\pi^+(X)$ control sample (*D_s^+ decay model*). These weights are varied by taking into account their uncertainties and correlations and the signal fit is repeated with the varied D_s^+ templates. Different corrections have been applied to the templates of double-charm backgrounds in order to obtain the data simulation-corrected $\cos\theta_D$ distributions. For each correction a systematic uncertainty is assigned by varying the corresponding weights within their uncertainty (*Shape of $\cos\theta_D$ template in D^*D decays*).

Another source of systematic uncertainty is related to the limited size of the simulated

Table 4: Values of a_{θ_D} , c_{θ_D} and $F_L^{D^*}$ from the fit.

Parameter	$q^2 < 7 \text{ GeV}^2/c^4$	$q^2 > 7 \text{ GeV}^2/c^4$	Whole q^2 range
a_{θ_D}	0.12 ± 0.02	0.16 ± 0.03	0.15 ± 0.03
c_{θ_D}	0.14 ± 0.05	0.01 ± 0.02	0.06 ± 0.06
$F_L^{D^*}$	0.52 ± 0.07	0.34 ± 0.08	0.41 ± 0.06

sample available for building the fit templates for the various components (*Limited template statistics*). This systematic uncertainty is evaluated repeating the fit using alternative templates obtained after resampling the baseline ones by means of a bootstrap technique. The usage of the ReDecay [44] technique in the generation of large simulated samples helps to keep this effect well under control.

The baseline fit strategy is compared to an alternative method using three-dimensional templates including the τ decay time, the anti- D_s^+ BDT output and q^2 . The fit results are projected in the $\cos\theta_D$ variable and a background subtraction is performed. Finally the $\cos\theta_D$ distribution, corrected for reconstruction effects, is fitted using a second-order polynomial for determining the a_{θ_D} and c_{θ_D} parameters. The results are found to be compatible with the baseline strategy and no systematic uncertainty is assigned.

Finally, an additional systematic uncertainty has been assigned for the determination of the $F_L^{D^*}$ value in the whole q^2 region. The bin efficiencies used for determining the integrated $F_L^{D^*}$ value are varied by one standard deviation and the difference with respect to the baseline value is taken as systematic uncertainty ($F_L^{D^*}$ integration method).

Table 5: Summary of the systematic uncertainties related to the D^{*-} polarization measurement.

Source	Low- q^2	High- q^2	Whole q^2 range
Fit validation	0.003	0.002	0.003
FF model	0.007	0.003	0.005
FF parameters	0.013	0.006	0.011
Limited template statistics	0.026	0.017	0.019
Fraction of signal $\tau^+ \rightarrow \pi^+ \pi^- \pi^+ \pi^0 \nu_\tau$ decays	0.001	0.001	0.001
Fraction of D^{**} feed-down	0.001	0.004	0.003
Signal selection	0.005	0.004	0.005
Bin migration	0.008	0.006	0.007
$F_L^{D^*}$ in simulation	0.007	0.003	0.007
D_s^+ decay model	0.008	0.009	0.009
Shape of $\cos\theta_D$ template in $D^{*-} D_s^+$ decays	0.002	0.001	0.002
Shape of $\cos\theta_D$ template in $D^{*-} D_s^{*+}$ decays	0.007	0.002	0.004
Shape of $\cos\theta_D$ template in $D^{*-} D_s^+ X$ decays	0.007	0.006	0.007
Shape of $\cos\theta_D$ template in $D^{*-} D^+ X$ decays	0.002	0.002	0.003
Shape of $\cos\theta_D$ template in $D^{*-} D^0 X$ decays	0.002	0.002	0.003
$F_L^{D^*}$ integration method	-	-	0.002
Total	0.035	0.023	0.029

8 Conclusions

A measurement of the D^{*-} longitudinal polarization fraction in $B^0 \rightarrow D^{*-} \tau^+ \nu_\tau$ decays was performed by the LHCb Collaboration using data collected at center-of-mass energies of 7, 8 and 13 TeV and corresponding to an integrated luminosity of 5 fb^{-1} . The $F_L^{D^*}$

value was measured in two q^2 bins and in the whole q^2 range, yielding

$$\begin{aligned} q^2 < 7 \text{ GeV}^2/c^4 & : & 0.52 \pm 0.07 \text{ (stat)} \pm 0.04 \text{ (syst)}, \\ q^2 > 7 \text{ GeV}^2/c^4 & : & 0.34 \pm 0.08 \text{ (stat)} \pm 0.02 \text{ (syst)}, \\ q^2 \text{ whole range} & : & 0.41 \pm 0.06 \text{ (stat)} \pm 0.03 \text{ (syst)}. \end{aligned}$$

The total correlation between the $F_L^{D^*}$ values in the two q^2 regions, considering both statistical and systematic effects, was found to be -0.18 . These measurements are compatible with SM predictions and with the results obtained by the Belle experiment [15].

Acknowledgments

We express our gratitude to our colleagues in the CERN accelerator departments for the excellent performance of the LHC. We thank the technical and administrative staff at the LHCb institutes. We acknowledge support from CERN and from the national agencies: CAPES, CNPq, FAPERJ and FINEP (Brazil); MOST and NSFC (China); CNRS/IN2P3 (France); BMBF, DFG and MPG (Germany); INFN (Italy); NWO (Netherlands); MNiSW and NCN (Poland); MCID/IFA (Romania); MICINN (Spain); SNSF and SER (Switzerland); NASU (Ukraine); STFC (United Kingdom); DOE NP and NSF (USA). We acknowledge the computing resources that are provided by CERN, IN2P3 (France), KIT and DESY (Germany), INFN (Italy), SURF (Netherlands), PIC (Spain), GridPP (United Kingdom), CSCS (Switzerland), IFIN-HH (Romania), CBPF (Brazil), Polish WLCG (Poland) and NERSC (USA). We are indebted to the communities behind the multiple open-source software packages on which we depend. Individual groups or members have received support from ARC and ARDC (Australia); Key Research Program of Frontier Sciences of CAS, CAS PIFI, CAS CCEPP, Fundamental Research Funds for the Central Universities, and Sci. & Tech. Program of Guangzhou (China); Minciencias (Colombia); EPLANET, Marie Skłodowska-Curie Actions, ERC and NextGenerationEU (European Union); A*MIDEX, ANR, IPhU and Labex P2IO, and Région Auvergne-Rhône-Alpes (France); AvH Foundation (Germany); ICSC (Italy); GVA, XuntaGal, GENCAT, Inditex, InTalent and Prog. Atracción Talento, CM (Spain); SRC (Sweden); the Leverhulme Trust, the Royal Society and UKRI (United Kingdom).

References

- [1] M. A. Ivanov, J. G. Körner, and C. T. Tran, *Exclusive decays $B \rightarrow \ell^- \bar{\nu}$ and $B \rightarrow D^{(*)} \ell^- \bar{\nu}$ in the covariant quark model*, Phys. Rev. **D92** (2015) 114022, [arXiv:1508.02678](#).
- [2] S. Fajfer, J. F. Kamenik, and I. Nišandžić, *On the $B \rightarrow D^* \tau \bar{\nu}_\tau$ sensitivity to new physics*, Phys. Rev. **D85** (2012) 094025, [arXiv:1203.2654](#).
- [3] BaBar collaboration, J. P. Lees *et al.*, *Evidence for an excess of $\bar{B} \rightarrow D^{(*)} \tau^- \bar{\nu}_\tau$ decays*, Phys. Rev. Lett. **109** (2012) 101802, [arXiv:1205.5442](#).
- [4] BaBar collaboration, B. Aubert *et al.*, *Observation of the semileptonic decays $B \rightarrow D^* \tau^- \bar{\nu}_\tau$ and evidence for $B \rightarrow D \tau^- \bar{\nu}_\tau$* , Phys. Rev. Lett. **100** (2008) 021801, [arXiv:0709.1698](#).

- [5] Belle collaboration, M. Huschle *et al.*, *Measurement of the branching ratio of $\bar{B} \rightarrow D^{(*)}\tau^-\bar{\nu}_\tau$ relative to $\bar{B} \rightarrow D^{(*)}\ell^-\bar{\nu}_\ell$ decays with hadronic tagging at Belle*, Phys. Rev. **D92** (2015) 072014, [arXiv:1507.03233](#).
- [6] Belle collaboration, A. Matyja *et al.*, *Observation of $B^0 \rightarrow D^{*-}\tau^+\nu_\tau$ decay at Belle*, Phys. Rev. Lett. **99** (2007) 191807, [arXiv:0706.4429](#).
- [7] Belle collaboration, Y. Sato *et al.*, *Measurement of the branching ratio of $\bar{B}^0 \rightarrow D^{*+}\tau^-\bar{\nu}_\tau$ relative to $\bar{B}^0 \rightarrow D^{*+}\ell^-\bar{\nu}_\ell$ decays with a semileptonic tagging method*, Phys. Rev. **D94** (2016) 072007, [arXiv:1607.07923](#).
- [8] Belle collaboration, S. Hirose *et al.*, *Measurement of the τ lepton polarization and $R(D^*)$ in the decay $\bar{B} \rightarrow D^*\tau^-\bar{\nu}_\tau$ with one-prong hadronic τ decays at Belle*, Phys. Rev. **D97** (2018) 012004, [arXiv:1709.00129](#).
- [9] LHCb collaboration, R. Aaij *et al.*, *Measurement of the ratio of the $\mathcal{B}(B^0 \rightarrow D^{*-}\tau^+\nu_\tau)$ and $\mathcal{B}(B^0 \rightarrow D^{*-}\mu^+\nu_\mu)$ branching fractions using three-prong τ -lepton decays*, Phys. Rev. Lett. **120** (2018) 171802, [arXiv:1708.08856](#).
- [10] LHCb collaboration, R. Aaij *et al.*, *Test of lepton flavor universality by the measurement of the $B^0 \rightarrow D^{*-}\tau^+\nu_\tau$ branching fraction using three-prong τ decays*, Phys. Rev. **D97** (2018) 072013, [arXiv:1711.02505](#).
- [11] LHCb collaboration, R. Aaij *et al.*, *Measurement of the ratio of branching fractions $\mathcal{R}(D^*)$ and $\mathcal{R}(D^0)$* , Phys. Rev. Lett. **131** (2023) 111802, [arXiv:2302.02886](#).
- [12] LHCb collaboration, R. Aaij *et al.*, *Test of lepton flavour universality using $B^0 \rightarrow D^{*-}\tau^+\nu_\tau$ decays, with hadronic τ channels*, Phys. Rev. **D108** (2023) 012018, Erratum *ibid.* **D109** (2024) 119902, [arXiv:2305.01463](#).
- [13] Y. Amhis *et al.*, *Averages of b -hadron, c -hadron, and τ -lepton properties as of 2021*, Phys. Rev. **D107** (2023) 052008, [arXiv:2206.07501](#), results and plots updated to winter 2024 available at <https://hflav.web.cern.ch>.
- [14] M. A. Ivanov, J. G. Körner, and C. T. Tran, *Analyzing new physics in the decays $\bar{B}^0 \rightarrow D^{(*)}\tau^-\bar{\nu}_\tau$ with form factors obtained from the covariant quark model*, Phys. Rev. **D94** (2016) 094028, [arXiv:1607.02932](#).
- [15] Belle collaboration, A. Abdesselam *et al.*, *Measurement of the D^{*-} polarization in the decay $B^0 \rightarrow D^{*-}\tau^+\nu_\tau$, in 10th International Workshop on the CKM Unitarity Triangle*, 2019, [arXiv:1903.03102](#).
- [16] M. Tanaka and R. Watanabe, *New physics in the weak interaction of $\bar{B} \rightarrow D^{(*)}\tau\bar{\nu}$* , Phys. Rev. **D87** (2013) 034028, [arXiv:1212.1878](#).
- [17] A. K. Alok, D. Kumar, S. Kumbhakar, and S. U. Sankar, *D^* polarization as a probe to discriminate new physics in $\bar{B} \rightarrow D^*\tau\bar{\nu}$* , Phys. Rev. **D95** (2017) 115038, [arXiv:1606.03164](#).
- [18] Z.-R. Huang *et al.*, *Footprints of new physics in $b \rightarrow c\tau\nu$ transitions*, Phys. Rev. **D98** (2018) 095018, [arXiv:1808.03565](#).

- [19] P. Colangelo and F. De Fazio, *Scrutinizing $\bar{B} \rightarrow D^* (D\pi) \ell^- \bar{\nu}_\ell$ and $\bar{B} \rightarrow D^* (D\gamma) \ell^- \bar{\nu}_\ell$ in search of new physics footprints*, JHEP **06** (2018) 082, [arXiv:1801.10468](#).
- [20] S. Bhattacharya, S. Nandi, and S. K. Patra, *$b \rightarrow c\tau\nu$ decays: a catalogue to compare, constrain, and correlate new physics effects*, Eur. Phys. J. **C79** (2019), [arXiv:1805.08222](#).
- [21] M. Bordone, N. Gubernari, D. van Dyk, and M. Jung, *Heavy-quark expansion for $\bar{B}_s \rightarrow D_s^{(*)}$ form factors and unitarity bounds beyond the $SU(3)_F$ limit*, Eur. Phys. J. **C80** (2020), [arXiv:1912.09335](#).
- [22] I. Ray and S. Nandi, *Test of new physics effects in $\bar{B} \rightarrow (D^{(*)}, \pi) \ell^- \bar{\nu}_\ell$ decays with heavy and light leptons*, [arXiv:2305.11855](#).
- [23] G. Martinelli, S. Simula, and L. Vittorio, *Updates on the determination of $|V_{cb}|$, $R(D^*)$ and $|V_{ub}|/|V_{cb}|$* , [arXiv:2310.03680](#).
- [24] D. Bečirević, M. Fedele, I. Nišandžić, and A. Tayduganov, *Lepton flavor universality tests through angular observables of $\bar{B} \rightarrow D^{(*)} \ell \bar{\nu}$ decay modes*, [arXiv:1907.02257](#).
- [25] LHCb collaboration, A. A. Alves Jr. *et al.*, *The LHCb detector at the LHC*, JINST **3** (2008) S08005.
- [26] LHCb collaboration, R. Aaij *et al.*, *LHCb detector performance*, Int. J. Mod. Phys. **A30** (2015) 1530022, [arXiv:1412.6352](#).
- [27] R. Aaij *et al.*, *Performance of the LHCb Vertex Locator*, JINST **9** (2014) P09007, [arXiv:1405.7808](#).
- [28] R. Arink *et al.*, *Performance of the LHCb Outer Tracker*, JINST **9** (2014) P01002, [arXiv:1311.3893](#).
- [29] P. d'Argent *et al.*, *Improved performance of the LHCb Outer Tracker in LHC Run 2*, JINST **12** (2017) P11016, [arXiv:1708.00819](#).
- [30] M. Adinolfi *et al.*, *Performance of the LHCb RICH detector at the LHC*, Eur. Phys. J. **C73** (2013) 2431, [arXiv:1211.6759](#).
- [31] A. A. Alves Jr. *et al.*, *Performance of the LHCb muon system*, JINST **8** (2013) P02022, [arXiv:1211.1346](#).
- [32] R. Aaij *et al.*, *The LHCb trigger and its performance in 2011*, JINST **8** (2013) P04022, [arXiv:1211.3055](#).
- [33] V. V. Gligorov and M. Williams, *Efficient, reliable and fast high-level triggering using a bonsai boosted decision tree*, JINST **8** (2013) P02013, [arXiv:1210.6861](#).
- [34] T. Likhomanenko *et al.*, *LHCb topological trigger reoptimization*, J. Phys. Conf. Ser. **664** (2015) 082025.



















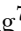









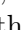





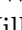
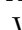

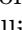
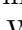
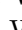

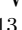




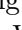
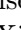




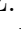







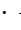


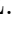
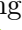





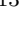

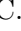

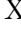
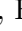
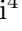



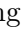


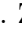

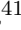
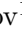









- [35] T. Sjöstrand, S. Mrenna, and P. Skands, *A brief introduction to PYTHIA 8.1*, Comput. Phys. Commun. **178** (2008) 852, [arXiv:0710.3820](#); T. Sjöstrand, S. Mrenna, and P. Skands, *PYTHIA 6.4 physics and manual*, JHEP **05** (2006) 026, [arXiv:hep-ph/0603175](#).
- [36] I. Belyaev *et al.*, *Handling of the generation of primary events in Gauss, the LHCb simulation framework*, J. Phys. Conf. Ser. **331** (2011) 032047.
- [37] D. J. Lange, *The EvtGen particle decay simulation package*, Nucl. Instrum. Meth. **A462** (2001) 152.
- [38] N. Davidson, T. Przedzinski, and Z. Was, *PHOTOS interface in C++: Technical and physics documentation*, Comp. Phys. Comm. **199** (2016) 86, [arXiv:1011.0937](#).
- [39] I. M. Nugent *et al.*, *Resonance chiral lagrangian currents and experimental data for $\tau^- \rightarrow \pi^- \pi^- \pi^+ \nu_\tau$* , Phys. Rev. **D88** (2013) 093012, [arXiv:1310.1053](#).
- [40] N. Davidson *et al.*, *Universal interface of TAUOLA: Technical and physics documentation*, Comp. Phys. Comm. **183** (2012) 821, [arXiv:1002.0543](#).
- [41] I. M. Nugent, *Invariant mass spectra of $\tau^- \rightarrow h^- h^- h^+ \nu_\tau$ decays*, Nuclear Physics B - Proceedings Supplements **253-255** (2014) 38, [arXiv:1301.7105](#).
- [42] Geant4 collaboration, J. Allison *et al.*, *Geant4 developments and applications*, IEEE Trans. Nucl. Sci. **53** (2006) 270; Geant4 collaboration, S. Agostinelli *et al.*, *Geant4: A simulation toolkit*, Nucl. Instrum. Meth. **A506** (2003) 250.
- [43] M. Clemencic *et al.*, *The LHCb simulation application, Gauss: Design, evolution and experience*, J. Phys. Conf. Ser. **331** (2011) 032023.
- [44] D. Müller, M. Clemencic, G. Corti, and M. Gersabeck, *ReDecay: A novel approach to speed up the simulation at LHCb*, Eur. Phys. J. **C78** (2018) 1009, [arXiv:1810.10362](#).
- [45] L. Breiman, J. H. Friedman, R. A. Olshen, and C. J. Stone, *Classification and regression trees*, Wadsworth international group, Belmont, California, USA, 1984.
- [46] Y. Freund and R. E. Schapire, *A decision-theoretic generalization of on-line learning and an application to boosting*, J. Comput. Syst. Sci. **55** (1997) 119.
- [47] A. Hoecker *et al.*, *TMVA 4 — Toolkit for Multivariate Data Analysis with ROOT. Users Guide.*, [arXiv:physics/0703039](#).
- [48] I. Caprini, L. Lellouch, and M. Neubert, *Dispersive bounds on the shape of $B \rightarrow D^{(*)} \ell \nu$ form factors*, Nuclear Physics **B530** (1998) 153–181, [arXiv:hep-ph/9712417](#).
- [49] F. U. Bernlochner *et al.*, *Das ist der HAMMER: Consistent new physics interpretations of semileptonic decays*, Eur. Phys. J. **C80** (2020) 883, [arXiv:2002.00020](#).
- [50] J. G. Pardiñas *et al.*, *RooHammerModel: interfacing the HAMMER software tool with HistFactory and RooFit*, JINST **17** (2022) T04006, [arXiv:2007.12605](#).
- [51] M. Pivk and F. R. Le Diberder, *sPlot: A statistical tool to unfold data distributions*, Nucl. Instrum. Meth. **A555** (2005) 356, [arXiv:physics/0402083](#).

- [52] Particle Data Group, R. L. Workman *et al.*, *Review of particle physics*, Prog. Theor. Exp. Phys. **2022** (2022) 083C01.
- [53] F. U. Bernlochner, M. F. Sevilla, D. J. Robinson, and G. Wormser, *Semitaonic b -hadron decays: A lepton flavor universality laboratory*, Rev. Mod. Phys. **94** (2022) , arXiv:2101.08326.
- [54] C. G. Boyd, B. Grinstein, and R. F. Lebed, *Precision corrections to dispersive bounds on form factors*, Phys. Rev. **D56** (1997) 6895, arXiv:hep-ph/9705252.
- [55] F. U. Bernlochner, Z. Ligeti, M. Papucci, and D. J. Robinson, *Combined analysis of semileptonic B decays to D and D^* : $R(D^{(*)})$, $|V_{cb}|$, and new physics*, Phys. Rev. **D95** (2017) , arXiv:1703.05330.

LHCb collaboration

R. Aaij³⁵ , A.S.W. Abdelmotteleb⁵⁴ , C. Abellan Beteta⁴⁸ , F. Abudinén⁵⁴ ,
T. Ackernley⁵⁸ , B. Adeva⁴⁴ , M. Adinolfi⁵² , P. Adlarson⁷⁸ , H. Afsharnia¹¹ ,
C. Agapopoulou⁴⁶ , C.A. Aidala⁷⁹ , Z. Ajaltouni¹¹ , S. Akar⁶³ , K. Akiba³⁵ ,
P. Albicocco²⁵ , J. Albrecht^{17,g} , F. Alessio⁴⁶ , M. Alexander⁵⁷ , A. Alfonso Albero⁴³ ,
Z. Aliouche⁶⁰ , P. Alvarez Cartelle⁵³ , R. Amalric¹⁵ , S. Amato³ , J.L. Amey⁵² ,
Y. Amhis^{13,46} , L. An⁶ , L. Anderlini²⁴ , M. Andersson⁴⁸ , A. Andreianov⁴¹ ,
P. Andreola⁴⁸ , M. Andreotti²³ , D. Andreou⁶⁶ , D. Ao⁷ , F. Archilli^{34,w} ,
S. Arguedas Cuendis⁹ , A. Artamonov⁴¹ , M. Artuso⁶⁶ , E. Aslanides¹² , M. Atzeni⁶² ,
B. Audurier¹⁴ , D. Bacher⁶¹ , I. Bachiller Perea¹⁰ , S. Bachmann¹⁹ , M. Bachmayer⁴⁷ ,
J.J. Back⁵⁴ , A. Bailly-reyre¹⁵ , P. Baladron Rodriguez⁴⁴ , V. Balagura¹⁴ ,
W. Baldini^{23,46} , J. Baptista de Souza Leite² , M. Barbetti^{24,n} , I. R. Barbosa⁶⁷ ,
R.J. Barlow⁶⁰ , S. Barsuk¹³ , W. Barter⁵⁶ , M. Bartolini⁵³ , F. Baryshnikov⁴¹ ,
J.M. Basels¹⁶ , G. Bassi^{32,t} , B. Batsukh⁵ , A. Battig¹⁷ , A. Bay⁴⁷ , A. Beck⁵⁴ ,
M. Becker¹⁷ , F. Bedeschi³² , I.B. Bediaga² , A. Beiter⁶⁶ , S. Belin⁴⁴ , V. Bellee⁴⁸ ,
K. Belous⁴¹ , I. Belov²⁶ , I. Belyaev⁴¹ , G. Benane¹² , G. Bencivenni²⁵ ,
E. Ben-Haim¹⁵ , A. Berezhnoy⁴¹ , R. Bernet⁴⁸ , S. Bernet Andres⁴² , D. Berninghoff¹⁹ ,
H.C. Bernstein⁶⁶ , C. Bertella⁶⁰ , A. Bertolin³⁰ , C. Betancourt⁴⁸ , F. Betti⁵⁶ , J.
Bex⁵³ , Ia. Bezshyiko⁴⁸ , J. Bhom³⁸ , L. Bian⁷¹ , M.S. Bieker¹⁷ , N.V. Biesuz²³ ,
P. Billoir¹⁵ , A. Biolchini³⁵ , M. Birch⁵⁹ , F.C.R. Bishop⁵³ , A. Bitadze⁶⁰ , A. Bizzeti ,
M.P. Blago⁵³ , T. Blake⁵⁴ , F. Blanc⁴⁷ , J.E. Blank¹⁷ , S. Blusk⁶⁶ , D. Bobulska⁵⁷ ,
V. Bocharnikov⁴¹ , J.A. Boelhave¹⁷ , O. Boente Garcia¹⁴ , T. Boettcher⁶³ , A.
Bohare⁵⁶ , A. Boldyrev⁴¹ , C.S. Bolognani⁷⁶ , R. Bolzonella^{23,m} , N. Bondar⁴¹ ,
F. Borgato^{30,r,46} , S. Borghi⁶⁰ , M. Borsato^{28,q} , J.T. Borsuk³⁸ , S.A. Bouchiba⁴⁷ ,
T.J.V. Bowcock⁵⁸ , A. Boyer⁴⁶ , C. Bozzi²³ , M.J. Bradley⁵⁹ , S. Braun⁶⁴ ,
A. Brea Rodriguez⁴⁴ , N. Breer¹⁷ , J. Brodzicka³⁸ , A. Brossa Gonzalo^{44,54,43,†} ,
J. Brown⁵⁸ , D. Brundu²⁹ , A. Buonauro⁴⁸ , L. Buonincontri^{30,r} , A.T. Burke⁶⁰ ,
C. Burr⁴⁶ , A. Bursche⁶⁹ , A. Butkevich⁴¹ , J.S. Butter⁵³ , J. Buytaert⁴⁶ ,
W. Byczynski⁴⁶ , S. Cadeddu²⁹ , H. Cai⁷¹ , R. Calabrese^{23,m} , L. Calefice¹⁷ , S. Cali²⁵ ,
M. Calvi^{28,q} , M. Calvo Gomez⁴² , J. I. Cambon Bouzas⁴⁴ , P. Campana²⁵ ,
D.H. Campora Perez⁷⁶ , A.F. Campoverde Quezada⁷ , S. Capelli^{28,q} , L. Capriotti²³ ,
A. Carbone^{22,k} , L. Carcedo Salgado⁴⁴ , R. Cardinale^{26,o} , A. Cardini²⁹ , P. Carniti^{28,q} ,
L. Carus¹⁹ , A. Casais Vidal⁴⁴ , R. Caspary¹⁹ , G. Casse⁵⁸ , J. Castro Godinez⁹ ,
M. Cattaneo⁴⁶ , G. Cavallero^{23,46} , V. Cavallini^{23,m} , S. Celani⁴⁷ , D. Cervenkov⁶¹ , S.
Cesare^{27,p} , A.J. Chadwick⁵⁸ , I. Chahrouh⁷⁹ , M.G. Chapman⁵² , M. Charles¹⁵ ,
Ph. Charpentier⁴⁶ , C.A. Chavez Barajas⁵⁸ , M. Chefdeville¹⁰ , C. Chen¹² , S. Chen⁵ ,
A. Chernov³⁸ , S. Chernyshenko⁵⁰ , V. Chobanova^{44,aa} , S. Cholak⁴⁷ , M. Chruszcz³⁸ ,
A. Chubykin⁴¹ , V. Chulikov⁴¹ , P. Ciambrome²⁵ , M.F. Cicala⁵⁴ , X. Cid Vidal⁴⁴ ,
G. Ciezarek⁴⁶ , P. Cifra⁴⁶ , P.E.L. Clarke⁵⁶ , M. Clemencic⁴⁶ , H.V. Cliff⁵³ ,
J. Closier⁴⁶ , J.L. Cobbledick⁶⁰ , C. Cocha Toapaxi¹⁹ , V. Coco⁴⁶ , J. Cogan¹² ,
E. Cogneras¹¹ , L. Cojocariu⁴⁰ , P. Collins⁴⁶ , T. Colombo⁴⁶ , A. Comerma-Montells⁴³ ,
L. Congedo²¹ , A. Contu²⁹ , N. Cooke⁵⁷ , I. Corredoira⁴⁴ , A. Correia¹⁵ , G. Corti⁴⁶ ,
J.J. Cottee Meldrum⁵² , B. Couturier⁴⁶ , D.C. Craik⁴⁸ , M. Cruz Torres^{2,i} , R. Currie⁵⁶ ,
C.L. Da Silva⁶⁵ , S. Dadabaev⁴¹ , L. Dai⁶⁸ , X. Dai⁶ , E. Dall'Occo¹⁷ , J. Dalseno⁴⁴ ,
C. D'Ambrosio⁴⁶ , J. Daniel¹¹ , A. Danilina⁴¹ , P. d'Argent²¹ , A. Davidson⁵⁴ ,
J.E. Davies⁶⁰ , A. Davis⁶⁰ , O. De Aguiar Francisco⁶⁰ , C. De Angelis^{29,l} , J. de Boer³⁵ ,
K. De Bruyn⁷⁵ , S. De Capua⁶⁰ , M. De Cian¹⁹ , U. De Freitas Carneiro Da Graca^{2,b} ,
E. De Lucia²⁵ , J.M. De Miranda² , L. De Paula³ , M. De Serio^{21,j} , D. De Simone⁴⁸ ,
P. De Simone²⁵ , F. De Vellis¹⁷ , J.A. de Vries⁷⁶ , F. Debernardis^{21,j} , D. Decamp¹⁰ 

V. Dedu¹² , L. Del Buono¹⁵ , B. Delaney⁶² , H.-P. Dembinski¹⁷ , J. Deng⁸ , V. Denysenko⁴⁸ , O. Deschamps¹¹ , F. Dettori^{29,l} , B. Dey⁷⁴ , P. Di Nezza²⁵ , I. Diachkov⁴¹ , S. Didenko⁴¹ , S. Ding⁶⁶ , V. Dobishuk⁵⁰ , A. D. Docheva⁵⁷ , A. Dolmatov⁴¹ , C. Dong⁴ , A.M. Donohoe²⁰ , F. Dordei²⁹ , A.C. dos Reis² , L. Douglas⁵⁷ , A.G. Downes¹⁰ , W. Duan⁶⁹ , P. Duda⁷⁷ , M.W. Dudek³⁸ , L. Dufour⁴⁶ , V. Duk³¹ , P. Durante⁴⁶ , M. M. Duras⁷⁷ , J.M. Durham⁶⁵ , D. Dutta⁶⁰ , A. Dziurda³⁸ , A. Dzyuba⁴¹ , S. Easo^{55,46} , E. Eckstein⁷³ , U. Egede¹ , A. Egorychev⁴¹ , V. Egorychev⁴¹ , C. Eirea Orro⁴⁴ , S. Eisenhardt⁵⁶ , E. Ejopu⁶⁰ , S. Ek-In⁴⁷ , L. Eklund⁷⁸ , M. Elashri⁶³ , J. Ellbracht¹⁷ , S. Ely⁵⁹ , A. Ene⁴⁰ , E. Epple⁶³ , S. Escher¹⁶ , J. Eschle⁴⁸ , S. Esen⁴⁸ , T. Evans⁶⁰ , F. Fabiano^{29,l,46} , L.N. Falcao² , Y. Fan⁷ , B. Fang^{71,13} , L. Fantini^{31,s} , M. Faria⁴⁷ , K. Farmer⁵⁶ , S. Farry⁵⁸ , D. Fazzini^{28,q} , L. Felkowski⁷⁷ , M. Feng^{5,7} , M. Feo⁴⁶ , M. Fernandez Gomez⁴⁴ , A.D. Ferez⁶⁴ , F. Ferrari²² , F. Ferreira Rodrigues³ , S. Ferreres Sole³⁵ , M. Ferrillo⁴⁸ , M. Ferro-Luzzi⁴⁶ , S. Filippov⁴¹ , R.A. Fini²¹ , M. Fiorini^{23,m} , M. Firlej³⁷ , K.L. Fischer⁶¹ , D.S. Fitzgerald⁷⁹ , C. Fitzpatrick⁶⁰ , T. Fiutowski³⁷ , F. Fleuret¹⁴ , M. Fontana²² , F. Fontanelli^{26,o} , L. F. Foreman⁶⁰ , R. Forty⁴⁶ , D. Foulds-Holt⁵³ , M. Franco Sevilla⁶⁴ , M. Frank⁴⁶ , E. Franzoso^{23,m} , G. Frau¹⁹ , C. Frei⁴⁶ , D.A. Friday⁶⁰ , L. Frontini²⁷ , J. Fu⁷ , Q. Führung^{17,g} , Y. Fujii¹ , T. Fulghesu¹⁵ , E. Gabriel³⁵ , G. Galati^{21,j} , M.D. Galati³⁵ , A. Gallas Torreira⁴⁴ , D. Galli^{22,k} , S. Gambetta^{56,46} , M. Gandelman³ , P. Gandini²⁷ , H. Gao⁷ , R. Gao⁶¹ , Y. Gao⁸ , Y. Gao⁶ , M. Garau^{29,l} , L.M. Garcia Martin⁴⁷ , P. Garcia Moreno⁴³ , J. García Pardiñas⁴⁶ , B. Garcia Plana⁴⁴ , F.A. Garcia Rosales¹⁴ , L. Garrido⁴³ , C. Gaspar⁴⁶ , R.E. Geertsema³⁵ , L.L. Gerken¹⁷ , E. Gersabeck⁶⁰ , M. Gersabeck⁶⁰ , T. Gershon⁵⁴ , Z. Ghorbanimoghaddam⁵² , L. Giambastiani^{30,r} , F. I. Giasemis^{15,f} , V. Gibson⁵³ , H.K. Giemza³⁹ , A.L. Gilman⁶¹ , M. Giovannetti²⁵ , A. Gioventù⁴³ , P. Gironella Gironell⁴³ , C. Giugliano^{23,m} , M.A. Giza³⁸ , K. Gizdov⁵⁶ , E.L. Gkougkousis⁵⁹ , F.C. Glaser^{13,19} , V.V. Gligorov¹⁵ , C. Göbel⁶⁷ , E. Golobardes⁴² , D. Golubkov⁴¹ , A. Golutvin^{59,41,46} , A. Gomes^{2,3,c,a,†} , S. Gomez Fernandez⁴³ , F. Goncalves Abrantes⁶¹ , M. Goncerz³⁸ , G. Gong⁴ , J. A. Gooding¹⁷ , I.V. Gorelov⁴¹ , C. Gotti²⁸ , J.P. Grabowski⁷³ , L.A. Granado Cardoso⁴⁶ , E. Graugés⁴³ , E. Graverini⁴⁷ , L. Grazette⁵⁴ , G. Graziani , A. T. Greco⁴⁰ , L.M. Greeven³⁵ , N.A. Grieser⁶³ , L. Grillo⁵⁷ , S. Gromov⁴¹ , C. Gu¹⁴ , M. Guarise²³ , M. Guittiere¹³ , V. Guliaeva⁴¹ , P. A. Günther¹⁹ , A.-K. Guseinov⁴¹ , E. Gushchin⁴¹ , Y. Guz^{6,41,46} , T. Gys⁴⁶ , T. Hadavizadeh¹ , C. Hadjivasiliou⁶⁴ , G. Haefeli⁴⁷ , C. Haen⁴⁶ , J. Haimberger⁴⁶ , S.C. Haines⁵³ , M. Hajheidari⁴⁶ , T. Halewood-leagas⁵⁸ , M.M. Halvorsen⁴⁶ , P.M. Hamilton⁶⁴ , J. Hammerich⁵⁸ , Q. Han⁸ , X. Han¹⁹ , S. Hansmann-Menzemer¹⁹ , L. Hao⁷ , N. Harnew⁶¹ , T. Harrison⁵⁸ , M. Hartmann¹³ , C. Hasse⁴⁶ , J. He^{7,e} , K. Heijhoff³⁵ , F. Hemmer⁴⁶ , C. Henderson⁶³ , R.D.L. Henderson^{1,54} , A.M. Hennequin⁴⁶ , K. Hennessy⁵⁸ , L. Henry⁴⁷ , J. Herd⁵⁹ , J. Heuel¹⁶ , A. Hicheur³ , D. Hill⁴⁷ , M. Hilton⁶⁰ , S.E. Hollitt¹⁷ , J. Horswill⁶⁰ , R. Hou⁸ , Y. Hou¹⁰ , N. Howarth⁵⁸ , J. Hu¹⁹ , J. Hu⁶⁹ , W. Hu⁶ , X. Hu⁴ , W. Huang⁷ , X. Huang⁷¹ , W. Hulsbergen³⁵ , R.J. Hunter⁵⁴ , M. Hushchyn⁴¹ , D. Hutchcroft⁵⁸ , P. Ibis¹⁷ , M. Idzik³⁷ , D. Ilin⁴¹ , P. Ilten⁶³ , A. Inglesi⁴¹ , A. Injukhin⁴¹ , A. Ishteev⁴¹ , K. Ivshin⁴¹ , R. Jacobsson⁴⁶ , H. Jage¹⁶ , S.J. Jaimes Elles^{45,72} , S. Jakobsen⁴⁶ , E. Jans³⁵ , B.K. Jashal⁴⁵ , A. Jawahery⁶⁴ , V. Jevtic¹⁷ , E. Jiang⁶⁴ , X. Jiang^{5,7} , Y. Jiang⁷ , Y. J. Jiang⁶ , M. John⁶¹ , D. Johnson⁵¹ , C.R. Jones⁵³ , T.P. Jones⁵⁴ , S. Joshi³⁹ , B. Jost⁴⁶ , N. Jurik⁴⁶ , I. Juszcak³⁸ , D. Kaminaris⁴⁷ , S. Kandybei⁴⁹ , Y. Kang⁴ , M. Karacson⁴⁶ , D. Karpenkov⁴¹ , M. Karpov⁴¹ , A. Kauniskangas⁴⁷ , J.W. Kautz⁶³ , F. Keizer⁴⁶ , D.M. Keller⁶⁶ , M. Kenzie⁵³ , T. Ketel³⁵ , B. Khanji⁶⁶ , A. Kharisova⁴¹ ,

D. Vieira⁶³ , M. Vieites Diaz⁴⁶ , X. Vilasis-Cardona⁴² , E. Vilella Figueras⁵⁸ ,
A. Villa²² , P. Vincent¹⁵ , F.C. Volle¹³ , D. vom Bruch¹² , V. Vorobyev⁴¹,
N. Voropaev⁴¹ , K. Vos⁷⁶ , C. Vrahas⁵⁶ , J. Walsh³² , E.J. Walton^{1,54} , G. Wan⁶ ,
C. Wang¹⁹ , G. Wang⁸ , J. Wang⁶ , J. Wang⁵ , J. Wang⁴ , J. Wang⁷¹ , M. Wang²⁷ ,
N. W. Wang⁷ , R. Wang⁵² , X. Wang⁶⁹ , Y. Wang⁸ , Z. Wang¹³ , Z. Wang⁴ ,
Z. Wang⁷ , J.A. Ward^{54,1} , N.K. Watson⁵¹ , D. Websdale⁵⁹ , Y. Wei⁶ ,
B.D.C. Westhenry⁵² , D.J. White⁶⁰ , M. Whitehead⁵⁷ , A.R. Wiederhold⁵⁴ ,
D. Wiedner¹⁷ , G. Wilkinson⁶¹ , M.K. Wilkinson⁶³ , M. Williams⁶² ,
M.R.J. Williams⁵⁶ , R. Williams⁵³ , F.F. Wilson⁵⁵ , W. Wislicki³⁹ , M. Witek³⁸ ,
L. Witola¹⁹ , C.P. Wong⁶⁵ , G. Wormser¹³ , S.A. Wotton⁵³ , H. Wu⁶⁶ , J. Wu⁸ ,
Y. Wu⁶ , Z. Wu⁷ , K. Wyllie⁴⁶ , S. Xian⁶⁹, Z. Xiang⁵ , Y. Xie⁸ , A. Xu³² , J. Xu⁷ ,
L. Xu⁴ , L. Xu⁴ , M. Xu⁵⁴ , Z. Xu¹¹ , Z. Xu⁷ , Z. Xu⁵ , D. Yang , S. Yang⁷ ,
X. Yang⁶ , Y. Yang^{26,o} , Z. Yang⁶ , Z. Yang⁶⁴ , V. Yeroshenko¹³ , H. Yeung⁶⁰ ,
H. Yin⁸ , C. Y. Yu⁶ , J. Yu⁶⁸ , X. Yuan⁵ , E. Zaffaroni⁴⁷ , M. Zavertyaev¹⁸ ,
M. Zdybal³⁸ , M. Zeng⁴ , C. Zhang⁶ , D. Zhang⁸ , J. Zhang⁷ , L. Zhang⁴ ,
S. Zhang⁶⁸ , S. Zhang⁶ , Y. Zhang⁶ , Y. Zhang⁶¹, Y. Z. Zhang⁴ , Y. Zhao¹⁹ ,
A. Zharkova⁴¹ , A. Zhelezov¹⁹ , X. Z. Zheng⁴ , Y. Zheng⁷ , T. Zhou⁶ , X. Zhou⁸ ,
Y. Zhou⁷ , V. Zhovkovska¹³ , L. Z. Zhu⁷ , X. Zhu⁴ , X. Zhu⁸ , Z. Zhu⁷ ,
V. Zhukov^{16,41} , J. Zhuo⁴⁵ , Q. Zou^{5,7} , S. Zucchelli^{22,k} , D. Zuliani^{30,r} , G. Zunica⁶⁰ .

¹*School of Physics and Astronomy, Monash University, Melbourne, Australia*

²*Centro Brasileiro de Pesquisas Físicas (CBPF), Rio de Janeiro, Brazil*

³*Universidade Federal do Rio de Janeiro (UFRJ), Rio de Janeiro, Brazil*

⁴*Center for High Energy Physics, Tsinghua University, Beijing, China*

⁵*Institute Of High Energy Physics (IHEP), Beijing, China*

⁶*School of Physics State Key Laboratory of Nuclear Physics and Technology, Peking University, Beijing, China*

⁷*University of Chinese Academy of Sciences, Beijing, China*

⁸*Institute of Particle Physics, Central China Normal University, Wuhan, Hubei, China*

⁹*Consejo Nacional de Rectores (CONARE), San Jose, Costa Rica*

¹⁰*Université Savoie Mont Blanc, CNRS, IN2P3-LAPP, Annecy, France*

¹¹*Université Clermont Auvergne, CNRS/IN2P3, LPC, Clermont-Ferrand, France*

¹²*Aix Marseille Univ, CNRS/IN2P3, CPPM, Marseille, France*

¹³*Université Paris-Saclay, CNRS/IN2P3, IJCLab, Orsay, France*

¹⁴*Laboratoire Leprince-Ringuet, CNRS/IN2P3, Ecole Polytechnique, Institut Polytechnique de Paris, Palaiseau, France*

¹⁵*LPNHE, Sorbonne Université, Paris Diderot Sorbonne Paris Cité, CNRS/IN2P3, Paris, France*

¹⁶*I. Physikalisches Institut, RWTH Aachen University, Aachen, Germany*

¹⁷*Fakultät Physik, Technische Universität Dortmund, Dortmund, Germany*

¹⁸*Max-Planck-Institut für Kernphysik (MPIK), Heidelberg, Germany*

¹⁹*Physikalisches Institut, Ruprecht-Karls-Universität Heidelberg, Heidelberg, Germany*

²⁰*School of Physics, University College Dublin, Dublin, Ireland*

²¹*INFN Sezione di Bari, Bari, Italy*

²²*INFN Sezione di Bologna, Bologna, Italy*

²³*INFN Sezione di Ferrara, Ferrara, Italy*

²⁴*INFN Sezione di Firenze, Firenze, Italy*

²⁵*INFN Laboratori Nazionali di Frascati, Frascati, Italy*

²⁶*INFN Sezione di Genova, Genova, Italy*

²⁷*INFN Sezione di Milano, Milano, Italy*

²⁸*INFN Sezione di Milano-Bicocca, Milano, Italy*

²⁹*INFN Sezione di Cagliari, Monserrato, Italy*

³⁰*INFN Sezione di Padova, Padova, Italy*

³¹*INFN Sezione di Perugia, Perugia, Italy*

³²*INFN Sezione di Pisa, Pisa, Italy*

- ³³ INFN Sezione di Roma La Sapienza, Roma, Italy
- ³⁴ INFN Sezione di Roma Tor Vergata, Roma, Italy
- ³⁵ Nikhef National Institute for Subatomic Physics, Amsterdam, Netherlands
- ³⁶ Nikhef National Institute for Subatomic Physics and VU University Amsterdam, Amsterdam, Netherlands
- ³⁷ AGH - University of Krakow, Faculty of Physics and Applied Computer Science, Kraków, Poland
- ³⁸ Henryk Niewodniczanski Institute of Nuclear Physics Polish Academy of Sciences, Kraków, Poland
- ³⁹ National Center for Nuclear Research (NCBJ), Warsaw, Poland
- ⁴⁰ Horia Hulubei National Institute of Physics and Nuclear Engineering, Bucharest-Magurele, Romania
- ⁴¹ Affiliated with an institute covered by a cooperation agreement with CERN
- ⁴² DS4DS, La Salle, Universitat Ramon Llull, Barcelona, Spain
- ⁴³ ICCUB, Universitat de Barcelona, Barcelona, Spain
- ⁴⁴ Instituto Galego de Física de Altas Enerxías (IGFAE), Universidade de Santiago de Compostela, Santiago de Compostela, Spain
- ⁴⁵ Instituto de Física Corpuscular, Centro Mixto Universidad de Valencia - CSIC, Valencia, Spain
- ⁴⁶ European Organization for Nuclear Research (CERN), Geneva, Switzerland
- ⁴⁷ Institute of Physics, Ecole Polytechnique Fédérale de Lausanne (EPFL), Lausanne, Switzerland
- ⁴⁸ Physik-Institut, Universität Zürich, Zürich, Switzerland
- ⁴⁹ NSC Kharkiv Institute of Physics and Technology (NSC KIPT), Kharkiv, Ukraine
- ⁵⁰ Institute for Nuclear Research of the National Academy of Sciences (KINR), Kyiv, Ukraine
- ⁵¹ School of Physics and Astronomy, University of Birmingham, Birmingham, United Kingdom
- ⁵² H.H. Wills Physics Laboratory, University of Bristol, Bristol, United Kingdom
- ⁵³ Cavendish Laboratory, University of Cambridge, Cambridge, United Kingdom
- ⁵⁴ Department of Physics, University of Warwick, Coventry, United Kingdom
- ⁵⁵ STFC Rutherford Appleton Laboratory, Didcot, United Kingdom
- ⁵⁶ School of Physics and Astronomy, University of Edinburgh, Edinburgh, United Kingdom
- ⁵⁷ School of Physics and Astronomy, University of Glasgow, Glasgow, United Kingdom
- ⁵⁸ Oliver Lodge Laboratory, University of Liverpool, Liverpool, United Kingdom
- ⁵⁹ Imperial College London, London, United Kingdom
- ⁶⁰ Department of Physics and Astronomy, University of Manchester, Manchester, United Kingdom
- ⁶¹ Department of Physics, University of Oxford, Oxford, United Kingdom
- ⁶² Massachusetts Institute of Technology, Cambridge, MA, United States
- ⁶³ University of Cincinnati, Cincinnati, OH, United States
- ⁶⁴ University of Maryland, College Park, MD, United States
- ⁶⁵ Los Alamos National Laboratory (LANL), Los Alamos, NM, United States
- ⁶⁶ Syracuse University, Syracuse, NY, United States
- ⁶⁷ Pontifícia Universidade Católica do Rio de Janeiro (PUC-Rio), Rio de Janeiro, Brazil, associated to ³
- ⁶⁸ School of Physics and Electronics, Hunan University, Changsha City, China, associated to ⁸
- ⁶⁹ Guangdong Provincial Key Laboratory of Nuclear Science, Guangdong-Hong Kong Joint Laboratory of Quantum Matter, Institute of Quantum Matter, South China Normal University, Guangzhou, China, associated to ⁴
- ⁷⁰ Lanzhou University, Lanzhou, China, associated to ⁵
- ⁷¹ School of Physics and Technology, Wuhan University, Wuhan, China, associated to ⁴
- ⁷² Departamento de Física, Universidad Nacional de Colombia, Bogota, Colombia, associated to ¹⁵
- ⁷³ Universität Bonn - Helmholtz-Institut für Strahlen und Kernphysik, Bonn, Germany, associated to ¹⁹
- ⁷⁴ Eotvos Lorand University, Budapest, Hungary, associated to ⁴⁶
- ⁷⁵ Van Swinderen Institute, University of Groningen, Groningen, Netherlands, associated to ³⁵
- ⁷⁶ Universiteit Maastricht, Maastricht, Netherlands, associated to ³⁵
- ⁷⁷ Tadeusz Kosciuszko Cracow University of Technology, Cracow, Poland, associated to ³⁸
- ⁷⁸ Department of Physics and Astronomy, Uppsala University, Uppsala, Sweden, associated to ⁵⁷
- ⁷⁹ University of Michigan, Ann Arbor, MI, United States, associated to ⁶⁶
- ⁸⁰ Université Paris-Saclay, Centre d'Etudes de Saclay (CEA), IRFU, Saclay, France, Gif-Sur-Yvette, France

^a Universidade de Brasília, Brasília, Brazil

^b Centro Federal de Educação Tecnológica Celso Suckow da Fonseca, Rio De Janeiro, Brazil

^c Universidade Federal do Triângulo Mineiro (UFTM), Uberaba-MG, Brazil

- ^d *Central South U., Changsha, China*
^e *Hangzhou Institute for Advanced Study, UCAS, Hangzhou, China*
^f *LIP6, Sorbonne Université, Paris, France*
^g *Lamarr Institute for Machine Learning and Artificial Intelligence, Dortmund, Germany*
^h *Excellence Cluster ORIGINS, Munich, Germany*
ⁱ *Universidad Nacional Autónoma de Honduras, Tegucigalpa, Honduras*
^j *Università di Bari, Bari, Italy*
^k *Università di Bologna, Bologna, Italy*
^l *Università di Cagliari, Cagliari, Italy*
^m *Università di Ferrara, Ferrara, Italy*
ⁿ *Università di Firenze, Firenze, Italy*
^o *Università di Genova, Genova, Italy*
^p *Università degli Studi di Milano, Milano, Italy*
^q *Università degli Studi di Milano-Bicocca, Milano, Italy*
^r *Università di Padova, Padova, Italy*
^s *Università di Perugia, Perugia, Italy*
^t *Scuola Normale Superiore, Pisa, Italy*
^u *Università di Pisa, Pisa, Italy*
^v *Università della Basilicata, Potenza, Italy*
^w *Università di Roma Tor Vergata, Roma, Italy*
^x *Università di Siena, Siena, Italy*
^y *Università di Urbino, Urbino, Italy*
^z *Universidad de Alcalá, Alcalá de Henares, Spain*
^{aa} *Universidade da Coruña, Coruña, Spain*
^{ab} *Department of Physics/Division of Particle Physics, Lund, Sweden*

[†] *Deceased*